The Astrophysical Journal Letters, 886:L17 (12pp), 2019 November 20 https://doi.org/10.3847/2041-8213/ab5226

Two Years of Nonthermal Emission from the Binary Neutron Star Merger GW170817: Rapid Fading of the Jet Afterglow and First Constraints on the Kilonova Fastest Ejecta

A. Hajela[1], R. Margutti[1,20], K. D. Alexander[1,21], A. Kathirgamaraju[2,3], A. Baldeschi[1], C. Guidorzi[4], D. Giannios[2], W. Fong[1], Y. Wu[5], A. MacFadyen[5], A. Paggi[6,7], E. Berger[8], P. K. Blanchard[1], R. Chornock[9], D. L. Coppejans[1], P. S. Cowperthwaite[10,22], T. Eftekhari[8], S. Gomez[8], G. Hosseinzadeh[8], T. Laskar[11], B. D. Metzger[12], M. Nicholl[13,14], K. Paterson[1], D. Radice[15,16], L. Sironi[17], G. Terreran[1], V. A. Villar[8], P. K. G. Williams[8,18], X. Xie[19], and J. Zrake[12]

[1] Center for Interdisciplinary Exploration and Research in Astrophysics and Department of Physics and Astronomy, Northwestern University, 2145 Sheridan Road, Evanston, IL 60208-3112, USA
[2] Department of Physics and Astronomy, Purdue University, 525 Northwestern Avenue, West Lafayette, IN 47907-2036, USA
[3] Department of Astronomy and Theoretical Astrophysics Center, University of California Berkeley, Berkeley, CA 94720, USA
[4] Dipartimento di Fisica, Università Ferrara, Via Paradiso 12, I-44100 Ferrara, Italy
[5] Center for Cosmology and Particle Physics, New York University, 726 Broadway, New York, NY 10003, USA
[6] INAF—Osservatorio Astrofisico di Torino, via Osservatorio 20, I-10025 Pino Torinese, Italy
[7] INFN—Istituto Nazionale di Fisica Nucleare, Sezione di Torino, via Pietro Giuria 1, I-10125 Turin, Italy
[8] Center for Astrophysics, Harvard & Smithsonian, 60 Garden Street, Cambridge, MA 02138-1516, USA
[9] Astrophysical Institute, Department of Physics and Astronomy, 251B Clippinger Lab, Ohio University, Athens, OH 45701, USA
[10] Observatories of the Carnegie Institute for Science, 813 Santa Barbara Street, Pasadena, CA 91101-1232, USA
[11] Department of Physics, University of Bath, Claverton Down, Bath, BA2 7AY, UK
[12] Department of Physics and Columbia Astrophysics Laboratory, Columbia University, New York, NY 10027, USA
[13] Institute for Astronomy, University of Edinburgh, Royal Observatory, Blackford Hill, EH9 3HJ, UK
[14] Birmingham Institute for Gravitational Wave Astronomy and School of Physics and Astronomy, University of Birmingham, Birmingham B15 2TT, UK
[15] Department of Physics, The Pennsylvania State University, University Park, PA 16802, USA
[16] Department of Astronomy & Astrophysics, The Pennsylvania State University, University Park, PA 16802, USA
[17] Department of Astronomy and Columbia Astrophysics Laboratory, Columbia University, New York, NY 10027, USA
[18] American Astronomical Society, 1667 K Street NW, Suite 800, Washington, DC 20006-1681, USA
[19] Mathematical Sciences and STAG Research Centre, University of Southampton, Southampton SO17 1BJ, UK
Received 2019 September 13; revised 2019 October 25; accepted 2019 October 25; published 2019 November 18

Abstract

We present *Chandra* and Very Large Array observations of GW170817 at ∼521–743 days post-merger, and a homogeneous analysis of the entire *Chandra* data set. We find that the late-time nonthermal emission follows the expected evolution of an off-axis relativistic jet, with a steep temporal decay $F_\nu \propto t^{-1.95\pm0.15}$ and power-law spectrum $F_\nu \propto \nu^{-0.575\pm0.007}$. We present a new method to constrain the merger environment density based on diffuse X-ray emission from hot plasma in the host galaxy and find $n \leqslant 9.6 \times 10^{-3}\,\mathrm{cm}^{-3}$. This measurement is independent from inferences based on jet afterglow modeling and allows us to partially solve for model degeneracies. The updated best-fitting model parameters with this density constraint are a fireball kinetic energy $E_0 = 1.5^{+3.6}_{-1.1} \times 10^{49}$ erg ($E_{\rm iso} = 2.1^{+6.4}_{-1.5} \times 10^{52}$ erg) and jet opening angle $\theta_0 = 5.9^{+1.0}_{-0.7}$ deg with characteristic Lorentz factor $\Gamma_j = 163^{+23}_{-43}$, expanding in a low-density medium with $n_0 = 2.5^{+4.1}_{-1.9} \times 10^{-3}\,\mathrm{cm}^{-3}$ and viewed $\theta_{\rm obs} = 30.4^{+4.0}_{-3.4}$ deg off-axis. The synchrotron emission originates from a power-law distribution of electrons with index $p = 2.15^{+0.01}_{-0.02}$. The shock microphysics parameters are constrained to $\epsilon_{\rm e} = 0.18^{+0.30}_{-0.13}$ and $\epsilon_{\rm B} = 2.3^{+16.0}_{-2.2} \times 10^{-3}$. Furthermore, we investigate the presence of X-ray flares and find no statistically significant evidence of $\geqslant 2.5\sigma$ of temporal variability at any time. Finally, we use our observations to constrain the properties of synchrotron emission from the deceleration of the fastest kilonova ejecta with energy $E_k^{\rm KN} \propto (\Gamma\beta)^{-\alpha}$ into the environment, finding that shallow stratification indexes $\alpha \leqslant 6$ are disfavored. Future radio and X-ray observations will refine our inferences on the fastest kilonova ejecta properties.

Unified Astronomy Thesaurus concepts: Gamma-ray bursts (629); Neutron stars (1108); X-ray transient sources (1852); Diffuse x-ray background (384); Radio transient sources (2008)

1. Introduction

Multimessenger observations of the binary neutron star (BNS) merger event GW170817 ushered us into a new era of systematic exploration of our universe with gravitational waves and electromagnetic emission (Abbott et al. 2017a, 2017b). Light from GW170817 has been detected across the electromagnetic spectrum, from the γ-rays to the radio wavelengths (Alexander et al. 2017, 2018; Blanchard et al. 2017; Chornock et al. 2017; Coulter et al. 2017; Cowperthwaite et al. 2017; Fong et al. 2017; Goldstein et al. 2017; Haggard et al. 2017; Hallinan et al. 2017; Kasliwal et al. 2017; Margutti et al. 2017, 2018; Nicholl et al. 2017; Savchenko et al. 2017; Troja et al. 2017; Valenti et al. 2017; Dobie et al. 2018; Lyman et al. 2018; Nynka et al. 2018; Ruan et al. 2018). While the radiation powering the thermal emission from the kilonova (KN) associated with the BNS merger peaked at $\delta t < 12$ days (e.g., Villar et al. 2017, their Figure 1) and faded below the detection threshold of current

[20] CIFAR Azrieli Global Scholar, Gravity & the Extreme Universe Program, 2019.
[21] NASA Einstein Fellow.
[22] NASA Hubble Fellow.

instrumentation at $\delta t \sim 70$ days (with the latest detections in the NIR; Villar et al. 2018; Kasliwal et al. 2019), the nonthermal emission from the off-axis structured relativistic jet is longer lived.

Here we present deep X-ray and radio observations of the nonthermal emission from GW170817 covering the period $\delta t \sim 521$–743 days with the *Chandra X-ray Observatory* (*Chandra*) and the Karl G. Jansky Very Large Array (VLA), together with a comprehensive reanalysis of the entire *Chandra* data set. These observations allow us to refine previous inferences on the physical properties of the relativistic outflow launched by the BNS merger, and the density of the environment where the outflow is expanding (Alexander et al. 2018; D'Avanzo et al. 2018; Dobie et al. 2018; Granot et al. 2018; Hotokezaka et al. 2018; Lazzati et al. 2018; Margutti et al. 2018; Mooley et al. 2018a, 2018b, 2018c; Troja et al. 2018, 2019; Fong et al. 2019; Ghirlanda et al. 2019; Lamb et al. 2019). Finally, we use these observations to put the first constraints on the properties of nonthermal synchrotron emission from the deceleration of the KN fastest ejecta (i.e., the KN afterglow; e.g., Nakar & Piran 2011; Kathirgamaraju et al. 2019a).

This Letter is organized as follows. We present the analysis of two recent *Chandra* observations at $\delta t \sim 582$ and $\delta t \sim 743$ days in Section 2, together with a homogeneous temporal and spectral reanalysis of the entire *Chandra* data set acquired in two years of monitoring of GW170817. New VLA observations of GW170817 at $\delta t > 500$ days are presented in Section 3. Section 4 is dedicated to the broadband modeling of the nonthermal emission from GW170817 within the boosted fireball framework of Wu & MacFadyen (2018). Constraints on the KN afterglow and the physical properties of the KN fastest ejecta are derived in Section 5. Conclusions are drawn in Section 6.

All times are measured with respect to the time of the gravitational-wave trigger, which is 2017 August 17 12:41:04 UT (Abbott et al. 2017a). Uncertainties are provided at the 1σ confidence level (c.l.) and upper limits at the 3σ c.l. unless otherwise stated. We adopt the luminosity distance of NGC 4993, the host galaxy of GW170817, $d = 40.7$ Mpc inferred by Cantiello et al. (2018).

2. X-Ray Data Analysis

The *Chandra* started observing GW170817 on 2017 August 19 ($\delta t \sim 2$ days after the merger). Here we use a uniform framework for data reduction to perform a temporal and spectral analysis of new observations acquired at $\delta t \sim 580$–740 days, and a reanalysis of the entire *Chandra* data set spanning $\delta t \sim 2$–356 days after the merger. This is fundamental to our analysis and enables us to consistently compare the fluxes, measure the ambient density of the merger environment, reliably search for temporal variability, and model the afterglow. The total exposure time across all observations is ∼731 ks (Table 1). The *Chandra* data set acquired at $\delta t \sim 582$ and ∼743 days is presented here for the first time. Previous *Chandra* observations of GW170817 have been presented by Margutti et al. (2017, 2018), Haggard et al. (2017), Troja et al. (2017, 2018), Alexander et al. (2018), Nynka et al. (2018), Ruan et al. (2018), Pooley et al. (2018), and Piro et al. (2019). Our analysis consistently accounts for the low-count statistics of the *Chandra* observations of GW170817 to accurately determine the model parameters and their uncertainties, as described in Margutti et al. (2017, 2018) and Alexander et al. (2018). We show the *XMM-Newton* (*XMM*) measurements from D'Avanzo et al. (2018) and Piro et al. (2019) in Figure 1 but we do not include these data in our modeling below to minimize the impact of systematic effects arising from, for instance, variability of the central active galactic nucleus (AGN) confused with GW170817 in the *XMM* point-spread function (PSF).

2.1. X-Ray Temporal Analysis of GW170817

We homogeneously reduced the entire *Chandra* data set acquired at $\delta t \sim 2$–743 days since the merger following the steps below. We reprocessed all the observations with the `repro` task within `CIAO` (v4.11; Fruscione et al. 2006) applying standard ACIS data filtering and using the latest calibration database (`CALDB`, v4.8.3). We performed blind point-source detection with `wavdetect` on individual observation IDs. The results are reported in Table 1. An X-ray source is blindly detected with `wavdetect` at a location consistent with GW170817 in all observations acquired at $9.2 \leqslant \delta t < 360$ days, with inferred 0.5–8 keV net count-rates reported in Table 1. No X-ray emission from GW170817 is detected at $\delta t \sim 2.3$ days, and our results are consistent with the earlier ones reported by Margutti et al. (2017). The X-ray counterpart of GW170817 is blindly detected with a very low significance ($<3\sigma$) in the individual observations acquired at the epochs corresponding to $\delta t \sim 581$–743 days (IDs 21322, 22157, 22158, 21372, 22736, 22736; PIs: Margutti, Fong, Troja; programs 20500299, 20500691). However, we note that GW170817 is blindly detected with significance $\geqslant 3\sigma$ when observations acquired around the same time are merged (grouped IDs in Table 1).

Motivated by the claim of significant temporal variability around ∼160 days by Piro et al. (2019), we searched for short timescale variability within each observation ID and for observations acquired within $\delta t/t \leqslant 0.03$ (i.e., grouped IDs in Table 1) by applying a multinomial test to the observed photon counts. The null hypothesis that we want to test is that of a constant source count-rate in a time interval $\Delta t_{\rm tot}$. We thus assigned to each time interval a probability proportional to the effective exposure time Δt_k within $\Delta t_{\rm tot}$, and computed the log-likelihood of the observed photon counts with respect to a multinomial distribution with $n = N_{\rm tot}$ (where n is the number of trials and $N_{\rm tot}$ is the total number of observed photons in $\Delta t_{\rm tot}$). We then generated 10^4 realizations of $N_{\rm tot}$ events distributed among Δt_k following a multinomial distribution with probabilities defined as above. For each $\Delta t_{\rm tot}$, the statistical significance of the evidence of a departure from our null hypothesis is quantified by the fraction of synthetic data sets that showed a log-likelihood value at least as extreme as the one observed. We applied the multinomial test to each observation ID and to grouped IDs in Table 1. For single IDs, $\Delta t_{\rm tot}$ is defined by the start and end of the *Chandra* observations and we divided $\Delta t_{\rm tot}$ into two halves, Δt_1 and Δt_2. For grouped IDs, $\Delta t_{\rm tot}$ encompasses the time interval defined by the beginning and end time of the first and last observation, respectively, and the values of Δt_k are naturally defined as the exposure times of each ID.

We find no evidence for departures from our null hypothesis in the entire sample of *Chandra* observations of GW170817, with a statistical significance of short timescale variability of the X-ray emission from GW170817 of $\geqslant 2.5\sigma$ (Gaussian equivalent). In particular, our results do not confirm the claim of temporal variability at the level of 3.3σ in the time interval $\Delta t_{\rm tot} = 153$–164 days by Piro et al. (2019). By applying the same method as in Piro et al. (2019) we find that we can reproduce their results only for their particular choice of time intervals ($\Delta t = 153.4$–157.2 days versus $\Delta t = 159.8$–163.8 days, without considering data acquired

Table 1
Results from Our Homogeneous Spectral Analysis of all the *Chandra* Observations of GW170817 Between 2.3 and 743 Days Since Merger

ObsID	Time Since Merger (days)	Significance σ	Exposure (ks)	Net Count Rate (0.5–8 keV) (10^{-4} cts s^{-1})	$N_{\rm H,int}$ 3σ Upper Limit (10^{22} cm^{-2})	Photon Index Γ	Absorbed Flux (0.3–10 keV) (10^{-15} erg cm^{-2} s^{-1})	Luminosity (0.3–10 keV) (10^{38} erg s^{-1})
18955	2.33	⋯	24.6	<1.2	⋯	2 (assumed)	<1.4	<3.4
19294	9.20	5.8	49.4	2.9 ± 0.8	<17.6	$0.91^{+0.94}_{-0.39}$	$6.85^{+3.20}_{-3.04}$	$13.50^{+6.31}_{-6.00}$
20728	15.38	7.2	46.7	3.8 ± 0.9	<6.1	$1.55^{+0.76}_{-0.33}$	$5.99^{+2.54}_{-1.02}$	$12.53^{+5.31}_{-2.14}$
18988	15.94	5.3	46.7	3.0 ± 0.8		$3.54^{+1.49}_{-0.44}$	$2.22^{+0.76}_{-0.35}$	$5.55^{+2.11}_{-1.95}$ $4.32^{+1.15}_{-0.56}$	$19.37^{+7.37}_{-6.80}$ $10.35^{+2.76}_{-1.35}$
20860	107.97	33.4	74.1	14.7 ± 1.4	<1.7	$1.48^{+0.22}_{-0.14}$	$25.19^{+1.63}_{-2.04}$	$52.20^{+3.38}_{-4.22}$
20861	111.06	14.9	24.7	14.1 ± 2.4		$1.67^{+0.44}_{-0.28}$	$1.52^{+0.17}_{-0.12}$	$21.07^{+6.38}_{-3.70}$ $24.24^{+2.09}_{-2.87}$	$44.87^{+13.60}_{-7.87}$ $50.48^{+4.35}_{-5.98}$
20936	153.55	22.5	31.8	18.6 ± 2.5	<1.2	$1.35^{+0.31}_{-0.19}$	$32.37^{+13.89}_{-8.83}$	$66.00^{+28.33}_{-18.00}$
20938	157.12	13.5	15.9	18.5 ± 3.5		$1.75^{+0.46}_{-0.24}$	$26.46^{+4.11}_{-6.17}$	$57.14^{+8.87}_{-13.33}$
20937	158.92	12.6	20.8	13.6 ± 2.6		$1.90^{+0.57}_{-0.26}$	$1.58^{+0.26}_{-0.15}$	$20.39^{+6.76}_{-2.00}$ $24.20^{+3.60}_{-1.71}$	$45.34^{+15.04}_{-4.44}$ $50.84^{+7.57}_{-3.59}$
20939	159.93	10.6	22.2	10.8 ± 2.3		$1.93^{+0.61}_{-0.40}$	$14.37^{+1.42}_{-1.75}$	$32.16^{+3.19}_{-3.91}$
20945	163.73	7.4	14.2	11.5 ± 2.9		$1.61^{+1.03}_{-0.42}$	$21.06^{+6.11}_{-7.56}$	$44.40^{+12.88}_{-15.94}$
21080	259.20	13.8	50.8	7.8 ± 1.3	<3.8	$1.62^{+0.44}_{-0.27}$	$11.40^{+1.86}_{-1.32}$	$24.11^{+3.93}_{-2.80}$
21090	260.78	14.8	46.0	8.3 ± 1.4		$1.52^{+0.35}_{-0.24}$	$1.57^{+0.29}_{-0.13}$	$13.06^{+4.58}_{-1.52}$ $12.21^{+2.88}_{-1.48}$	$27.22^{+9.53}_{-3.18}$ $25.61^{+6.04}_{-3.10}$
21371	358.61	11.1	67.2	5.0 ± 0.9	<3.9	$1.69^{+0.49}_{-0.34}$	$7.75^{+2.70}_{-0.73}$	$16.58^{+5.77}_{-1.56}$
21322	580.99	2.3	35.6	1.5 ± 0.7	<3.05	$0.95^{+1.73}_{-1.67}$	$5.43^{+2.54}_{-2.20}$	$11.11^{+5.19}_{-4.49}$
22157	581.94	2.7	38.2	1.6 ± 0.7		$1.38^{+1.09}_{-1.05}$	$1.28^{+1.04}_{-0.15}$	$2.75^{+2.20}_{-1.36}$ $3.25^{+0.85}_{-1.03}$	$5.82^{+2.43}_{-2.57}$ $7.07^{+1.86}_{-2.24}$
22158	583.60	2.0	24.9	1.5 ± 0.8		$1.59^{+2.82}_{-2.57}$	$5.75^{+3.78}_{-3.01}$	$12.53^{+8.24}_{-6.57}$
21372	740.31	2.2	40.0	<1.3	<11.4	⋯	⋯	⋯
22736	742.26	3.0	33.6	1.0 ± 0.4		$2.61^{+2.66}_{-2.01}$	$1.23^{+1.05}_{-1.03}$	$2.45^{+1.39}_{-1.62}$ $2.21^{+0.85}_{-0.79}$	$6.77^{+3.85}_{-4.49}$ $4.82^{+1.86}_{-1.71}$
22737	743.13	4.6	25.2	2.2 ± 0.9		$1.21^{+1.46}_{-1.45}$	$7.22^{+3.25}_{-2.95}$	$15.03^{+6.78}_{-6.15}$
Joint Fit	⋯	⋯	⋯	⋯	<0.69	$1.57^{+0.12}_{-0.07}$	⋯	⋯

Note. The reported photon indices, absorbed fluxes, and (unabsorbed) luminosities are calculated for $N_{\rm H,int} = 0$ cm^{-2}. At $\delta t > 400$ days the photon index Γ is not well constrained and we adopt $\Gamma = 1.57$ for the spectral calibration. The reported significance is for a blind (targeted) detection for $\delta t < 360$ days ($\delta t > 360$ days).

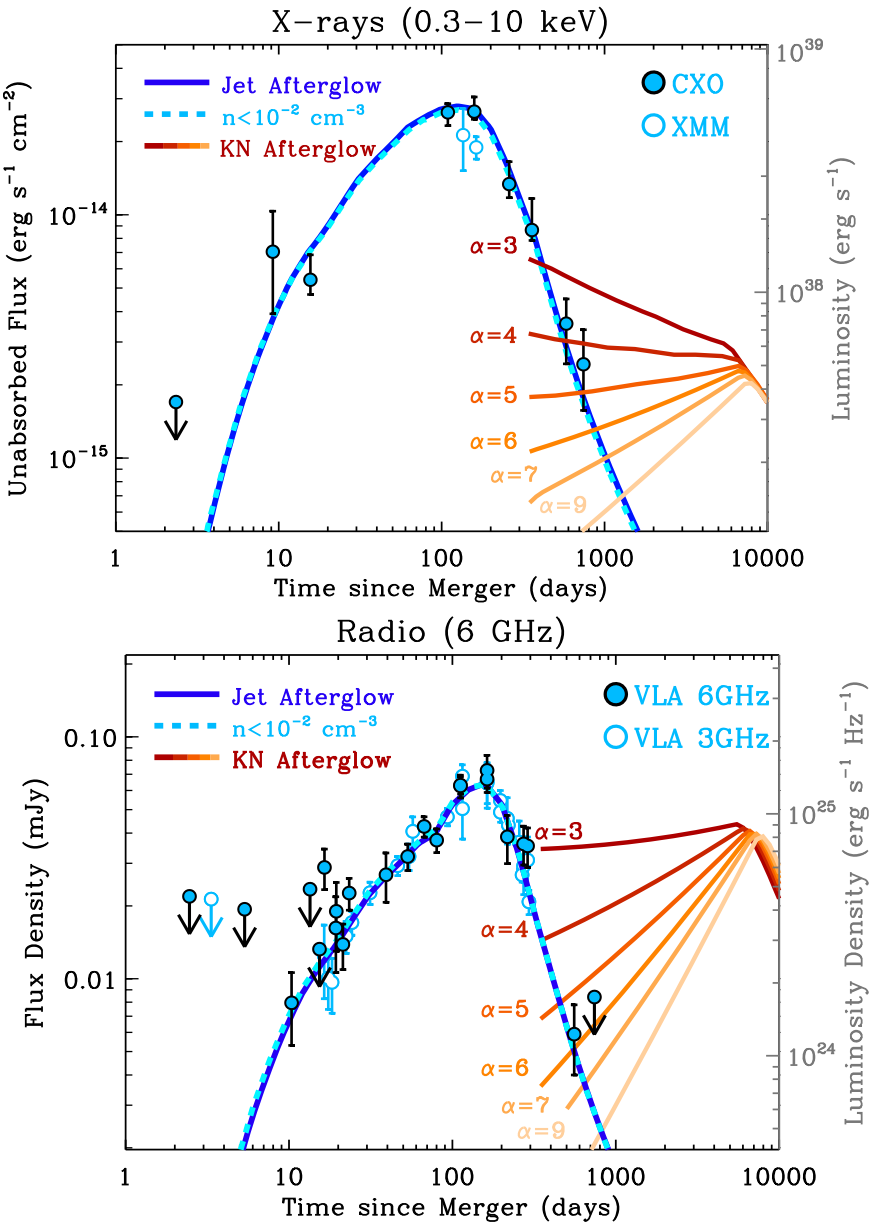

Figure 1. X-ray (upper panel) and radio (lower panel) emission from GW170817 in the first ∼743 days since merger as constrained by the *Chandra* (this work), *XMM-Newton* (D'Avanzo et al. 2018; Piro et al. 2019), and the most recent VLA observations (this work) merged with previous VLA observations (Alexander et al. 2017, 2018; Hallinan et al. 2017; Margutti et al. 2018; Mooley et al. 2018b, 2018c). We plot the VLA 6 GHz data (filled circles) and the 3 GHz data (empty circles) scaled at 6 GHz using an $F_\nu \propto \nu^{-0.6}$ spectrum. The broadband emission continues to be well modeled by a structured off-axis jet (solid blue line) with best-fitting energy $E_0 \sim 2 \times 10^{50}$ erg, $\theta_{\rm obs} \sim 33°$, $\theta_0 \sim 7°$ propagating into a medium with density $n \sim 0.07$ cm^{-3} (Section 4, Figure 3). Dashed light blue lines: best-fitting structured jet model for $n < 9.6 \times 10^{-3}$ cm^{-3} as derived in Section 2.3, which leads to $E_0 \sim 1.5 \times 10^{49}$ erg, $\theta_{\rm obs} \sim 30°$, $\theta_0 \sim 6°$ (Section 4, Figure 4). Thick red-to-orange lines: expected emission originating from the deceleration of the KN ejecta into the environment (i.e., the KN afterglow). We adopt the parameterization by Kathirgamaraju et al. (2019a) and show the expected KN afterglow emission for a set of representative values of the stratification index $\alpha = 3, 4, 5, 6, 7, 8, 9$ of the KN ejecta kinetic energy $E_k^{\rm KN}(>\Gamma\beta) \propto (\Gamma\beta)^{-\alpha}$, and for fiducial values of the microphysical parameters $\epsilon_B = 10^{-3}$, $\epsilon_e = 0.1$. We further adopt an environment density $n = 0.01$ cm^{-3} (the largest value allowed by our modeling of the diffuse X-ray emission, and a KN outflow with minimum velocity $v_0 \sim 0.3c$ and total energy $\sim 10^{51}$ erg, as found from the modeling of the UV–optical–NIR KN emission, which is sensitive to the slower moving ejecta that carries the bulk of the KN kinetic energy (e.g., Villar et al. 2017). Current observations constrain and disfavor the shallower $\alpha \lesssim 6$ values. Future broadband monitoring will probe a larger portion of the parameter space of the KN fastest ejecta (Section 5).

in *Chandra* ID 20937) and only if we do not account for the number of trials.[23] Properly accounting for the trials with the test above leads to reduced statistical evidence for temporal variability in this time interval of 1.8σ. We thus conclude that there is no statistical evidence for short-term variability in the X-ray afterglow of GW170817 and that the current *Chandra* data set does not quantitatively support the notion of an X-ray flare from a surviving magnetar remnant at $\delta t \sim 160$ days (Piro et al. 2019).

2.2. X-Ray Spectral Analysis of GW170817

For each observation ID we extracted a spectrum using `specextract` and a source region of 1.″5 centered at the

[23] Excluding the central portion of the data as in Piro et al. (2019), but allowing for a random selection of the initial and final time intervals to compare, leads to the conclusion that only ∼0.4% of blind choices would lead to a claim of temporal variability as significant as $\sim 3.3\sigma$ (see detailed discussion in Appendix A.1 and Figure 6).

location of the X-ray counterpart. We fitted each spectrum using an absorbed power-law model (tbabs*ztbabs*pow) within XSPEC (v12.9.1), adopting a Galactic neutral hydrogen column density $NH_{MW} = 0.0784 \times 10^{22}$ cm^{-2} (Kalberla et al. 2005). We employed Cash statistics and performed a series of Markov Chain Monte Carlo (MCMC) simulations to properly constrain the spectral parameters and their uncertainties in the regime of low-count statistics as in Margutti et al. (2017, 2018) and Alexander et al. (2018). In no case did we find any statistical evidence for significant intrinsic absorption $N_{H,int}$, and we list the derived 3σ upper limits in Table 1. We thus assume $N_{H,int} = 0$ cm^{-2} in our subsequent modeling. The inferred best-fitting photon indices Γ, absorbed fluxes, and (unabsorbed) luminosities are reported in Table 1. For observations acquired within a few days of each other, we also provide the results from a joint spectral fit and we plot the resulting lightcurve in Figure 1. Finally, we do not find statistical evidence for spectral evolution of the source over $\delta t \sim$ 2–743 days. From a joint fit of all the *Chandra* data at $\delta t \geqslant 9.2$ days we infer $N_{H,int} < 0.69 \times 10^{22}$ cm^{-2} and $\Gamma = 1.57^{+0.12}_{-0.07}$ (for $N_{H,int} = 0$ cm^{-2}), consistent with the spectral index inferred from broadband radio to X-ray studies (e.g., Alexander et al. 2018; Margutti et al. 2018; Troja et al. 2018; Fong et al. 2019).

2.3. Spatially Resolved Spectral Analysis of the Host Galaxy Diffuse X-Ray Emission

The host galaxy of GW170817 (NGC 4993) shows evidence for diffuse X-ray emission from a hot interstellar medium (ISM), in addition to harboring a weak AGN (e.g., Blanchard et al. 2017) and point sources of X-ray emission (Figure 2). In this section we describe the results from a spatially resolved X-ray spectral analysis of NGC 4993, with the goal to constrain the physical properties of the plasma responsible for the diffuse emission component, (i.e., plasma temperature T and particle density n), taking advantage of the very deep merged *Chandra* observation.

We followed the method developed by Paggi et al. (2014) to constrain the physical properties of the hot ISM of the elliptical galaxy NGC 4649. As a first step, we merged all the observations (with a total exposure time of ~731 ks) into a single event file using the merge_obs task within CIAO. merge_obs integrates two separate tasks: reproj_obs, which re-projects individual event files to a common astrometric solution, and flux_obs, which then merges the re-projected files into a single exposure-corrected event file. Other products from merge_obs include re-projected images, exposure maps, and exposure-corrected images in a given energy band. We then combined the PSF maps of individual observations into a single exposure-map weighted PSF file with dmimgcalc. Finally, we used the exposure-map weighted PSF file from the previous step, the merged re-projected 0.5–8 keV event file, and the exposure map created by merge_obs as input to wavdetect. Our goal was to detect faint point sources that would elude searches in individual exposures. We used a false-alert probability threshold of 4×10^{-6} and a set of different wavelet scales (i.e., 1, 2, 8, and 16). Visual inspection reveals that this method reliably identifies all the sources of pointlike X-ray emission in the merged image. The end product of this process is a list of detected point sources and corresponding point-source regions.

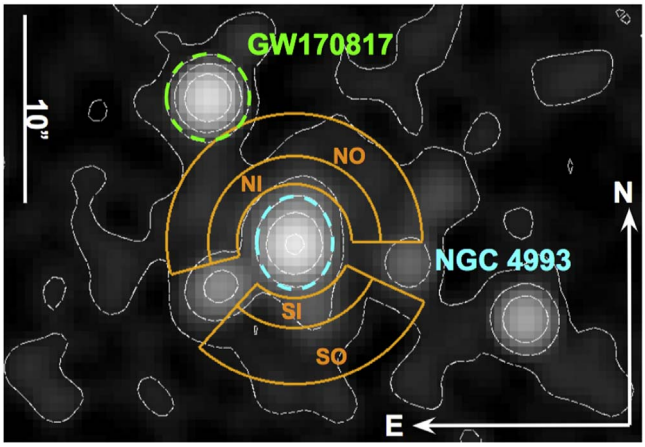

Figure 2. Combined X-ray image with *Chandra* observations from $\delta t \sim 2$ to 743 days post-merger in the 0.5–8 keV energy range, with contour levels in white. The four sectors in orange (NI: north inner, NO: north outer, SI: south inner, SO: south outer) mark the regions of spectra extraction for the spatially resolved X-ray spectral analysis of Section 2.3. The regions are defined so as to (i) exclude emission from the core of the host galaxy, (ii) avoid contamination from the neighboring point sources, and (iii) have a comparable number of background-subtracted counts.

We defined four regions for the extraction of the spectra of the diffuse X-ray emission as in Figure 2. The inner sectors (NI and SI in Figure 2) have an internal radius $r_{i,1} = 3\farcs5$ (to exclude the emission from the host-galaxy core, which is dominated by the AGN), an external radius $r_{e,1} = 5\farcs25$, and angular extents defined to avoid the point sources identified above. The north outer sector (NO in Figure 2) has an inner radius $r_{i,2} = r_{e,1}$ and extends to $r_{e,2} = 7\farcs8$ (near GW170817). The SO sector extends from $r_{e,1}$ to $r_{e,2} = 8\farcs7$. These regions are defined so as to contain the number of photons that leads to $\gtrsim 3\sigma$ evidence for emission in excess to the expected background counts, which corresponds to $N \sim$ 20–50 background-subtracted counts in the different regions.

For each observation ID, we extract four spectra with specextract (one for each of the sectors of Figure 2) with the background spectra extracted from the nearby "blank-sky" field, generating spectral response files that are weighted by the count distribution within the aperture, as appropriate for extended sources. Finally, for each sector, we combined the spectral files obtained in the previous step using combine_spectra.

We modeled the emission from hot plasma in NGC 4993 with the apec model within *Xspec*. Due to projection effects, each 2D sector in Figure 2 collects part of the radiation from 3D shells at larger radii. We accounted for these projection effects using the projct mixing model within *Xspec*, that is designed to perform a 3D to 2D projection of prolate ellipsoidal shells onto elliptical annuli (and respective sectors). We further adopted the solar abundances from Asplund et al. (2009) and fixed the metal abundance parameter of the apec model to three different values of $0.5\,Z_\odot$, $Z_\odot$, $2\,Z_\odot$, (where $Z_\odot$ is the solar metallicity). The galactic absorption column density was frozen to $NH_{MW} = 0.0784 \times 10^{22}$ cm^{-2} (Kalberla et al. 2005) for all the spectral fits. The fit was initially performed for the outermost sectors (NO and SO in Figure 2) independently, and the best-fitting parameters are reported in Table 2. The fit of the

Table 2
Best-fitting De-projected Emission Measure (EM) and Temperature T Derived from a Bremsstrahlung Spectral Fit of the Emission from the Concentric Annular Regions of Figure 2, and Derived Particle Density n

Shell	EM[a] ($\times 10^{-7}$ cm^{-5})	Temperature (T) (keV)	C-stat/dof	Density (n) ($\times 10^{-3}$ cm^{-3})
		$Z = 0.5\ Z_\odot$		
NO	$4.63^{+1.33}_{-0.79}$	$0.68^{+0.07}_{-0.11}$	386/510	$9.60^{+1.38}_{-0.82}$
NI	$12.41^{+3.59}_{-3.27}$	$2.03^{+1.49}_{-0.62}$	679/1022	$28.29^{+4.09}_{-3.73}$
SO	$2.71^{+1.14}_{-1.07}$	$1.83^{+3.62}_{-0.67}$	296/510	$7.68^{+1.62}_{-1.51}$
SI	$30.74^{+6.37}_{-5.55}$	$4.28^{+8.59}_{-1.84}$	539/1022	$58.06^{+6.02}_{-5.24}$
		$Z = Z_\odot$		
NO	$2.57^{+0.69}_{-0.45}$	$0.68^{+0.07}_{-0.11}$	385/510	$7.15^{+0.97}_{-0.69}$
NI	$9.72^{+3.08}_{-3.05}$	$2.18^{+1.81}_{-0.62}$	679/1022	$25.04^{+3.96}_{-3.93}$
SO	$2.36^{+1.07}_{-1.20}$	$2.67^{+4.65}_{-1.39}$	296/510	$7.16^{+1.63}_{-1.82}$
SI	$11.59^{+2.74}_{-2.41}$	$0.74^{+0.25}_{-0.16}$	547/1022	$35.66^{+4.21}_{-3.70}$
		$Z = 2\ Z_\odot$		
NO	$1.36^{+0.36}_{-0.24}$	$0.68^{+0.07}_{-0.11}$	385/510	$5.19^{+0.69}_{-0.46}$
NI	$7.03^{+2.79}_{-2.66}$	$2.43^{+2.09}_{-0.81}$	679/1022	$21.28^{+4.24}_{-4.02}$
SO	$2.15^{+0.84}_{-1.09}$	$4.29^{+3.68}_{-2.60}$	296/510	$7.37^{+1.56}_{-1.95}$
SI	$3.26^{+0.79}_{-0.64}$	$0.64^{+0.12}_{-0.11}$	490/1022	$18.90^{+2.29}_{-1.84}$

Note.
[a] $\mathrm{EM} = \frac{10^{-14}}{4\pi D_A^2}\int n_e n_{\rm H} dV$, where D_A is the angular diameter distance to the source (cm), n_e and $n_{\rm H}$ are the electron and H densities (cm^{-3}), respectively.

inner sectors were then performed jointly with their respective outer sectors, with the spectral parameters of the outer sectors frozen to the best-fitting parameters obtained in the previous step. All the resulting best-fitting de-projected model parameters (i.e., plasma temperature and emission measure, EM) for each sector are presented in Table 2 for three metallicity values.

2.3.1. Inferred Ionized Matter Density at the Location of GW170817

The best-fitting EM value of the `apec` diffuse emission model for the different shells provides a direct estimate of the host-galaxy density at that location. The EM is defined as

$$\mathrm{EM} = \frac{10^{-14}}{4\pi D_A^2}\int n_e n_{\rm H} dV \approx \frac{10^{-14}}{4\pi D_A^2}\left(\frac{\rho}{m_p}\right)^2 \frac{X(1+X)}{2} V_{\rm olume}, \quad (1)$$

where D_A is the angular distance to the host galaxy (in cm); n_e and $n_{\rm H}$ are the number density of electrons and hydrogen atoms (in cm^{-3}), respectively; and $n_e \sim \frac{\rho}{2m_p}(1+X)$. ρ is the matter density, X is the fraction of hydrogen by mass, and m_p is the proton mass. The particle densities inferred from the de-projected `apec` spectral fits are reported in Table 2. Of particular interest are the density values inferred for the outer sector NO. We find $n \sim (5.1\text{–}9.6) \times 10^{-3}$ cm^{-3}, depending on the assumed gas metallicity. GW170817 is located at a larger radius (Figure 2), where the gas density is likely to be lower. Additionally, unresolved point sources might contribute some of the detected emission. We thus consider $n \leqslant 9.6 \times 10^{-3}$ cm^{-3} as an upper limit on the density of ionized matter in the merger environment. Our density constraint analysis is not sensitive to the presence of small-scale density variations, for instance, the presence of overdensities at the edge of a bow-shock cavity formed if the merger progenitor hosted a pulsar (e.g., Ramirez-Ruiz et al. 2019). Our analysis complements previous inferences of neutral hydrogen particle density $n_{\rm H\,I} < 0.04$ cm^{-3} derived from radio observations by Hallinan et al. (2017), and it is consistent with the lower limit on the circum-merger density $n > 2 \times 10^{-5}$ cm^{-3} derived by Mooley et al. (2018b).

3. Radio Data Analysis

We observed GW170817 with the Karl G. Jansky VLA on 2019 January 21 beginning at 12:32:10 UT ($\delta t \sim 521$ days post-merger), 2019 January 25 at 10:52:45 UT ($\delta t \sim 525$ days), and 2019 March 29 at 05:00:15 UT ($\delta t \sim 588$ days). The January observations lasted 2 hr each and were taken in C configuration, while the March observation lasted 4 hr and was taken in B configuration. All observations were taken at a mean frequency of 6 GHz with an observing bandwidth of 4 GHz. The data were calibrated and imaged with standard CASA routines (McMullin et al. 2007), using 3C286 as the flux calibrator and J1258-2219 as the phase calibrator.

We do not detect GW170817 in any of the observations individually or in a combined image made from the two January observations. We therefore combine all three data sets using the CASA task `concat` and produce a single image with improved signal-to-noise. We recover a faint source at the location of GW170817 in the final joint image. We fit the emission with a point-source model using the `imtool` package within `pwkit` (Williams et al. 2017) and obtain a final flux density of 5.9 ± 1.9 μJy. This is consistent with expectations for an off-axis structured relativistic jet (Figure 1; Alexander et al. 2018; Wu & MacFadyen 2018; Xie et al. 2018).

A final epoch of radio observation was acquired at $\delta t = 724.3\text{–}743.2$ days since merger, and consisted of two observations, the first beginning on 2019 August 11 at 19:36:09 UT (3 hr, A configuration) and the second beginning on 2019 August 30 at 18:29:44 UT (3 hr, A configuration). For both observations the mean frequency is 6 GHz and the bandwidth is 4 GHz. Following the same data reduction and calibration procedure as above we do not find evidence of radio emission at the location of GW170817 in the individual observations or in a combined image. We also imaged the output of the observatory-provided NRAO pipeline calibrated data and obtained similar results. We infer $F_\nu < 8.4$ μJy at 3σ c.l. from the combined data set. We show the complete 6 GHz radio lightcurve of GW170817 in Figure 1.

The radio to X-ray spectral energy distribution at $\delta t \sim 582$ days is well modeled by a simple power law with $F_\nu \propto \nu^{-\beta}$ and $\beta = 0.55 \pm 0.02$ consistent with Fong et al. (2019) and the inferred broadband spectrum at earlier times (e.g., Alexander et al. 2018; D'Avanzo et al. 2018; Dobie et al. 2018; Margutti et al. 2018; Mooley et al. 2018a; Troja et al. 2018, 2019). We further infer a 3σ lower limit on the synchrotron cooling break frequency $\nu_c > 0.16$ keV at $\delta t \sim 582$ days. Based on data presented in this section and Section 2 we conclude that there is no evidence for spectral evolution of the nonthermal emission of GW170817 at any time of our monitoring, from $\delta t \sim 10$ days until ~740 days since merger.

4. Updated Modeling of the Broadband Jet Afterglow Emission

We use JetFit, the synthetic lightcurve fitting tool based on the two-parameter boosted fireball model developed by Duffell & MacFadyen (2013) and Wu & MacFadyen (2018), to fit the broadband nonthermal emission from GW170817 up to ∼2 yr since merger. JetFit can naturally accommodate a wide range of outflow structures ranging from mildly relativistic quasi-spherical outflows to ultrarelativistic structured jets (Wu & MacFadyen 2018, 2019). Specifically, our data set consists of the X-ray observations from Table 1, ∼3 and ∼6 GHz VLA radio observations collected from Alexander et al. (2017, 2018), Hallinan et al. (2017), Mooley et al. (2018a, 2018b), Margutti et al. (2018), and Dobie et al. (2018), as well as our latest radio observations presented in Section 3.

Within JetFit the synthetic lightcurves are generated using four hydrodynamical parameters: explosion energy E_0 (one side), ambient density n, asymptotic Lorentz factor η_0, and boost Lorentz factor γ_B; four radiative parameters: spectral index p of the electron distribution $N_e(\gamma_e) \propto \gamma_e^{-p}$, the electron energy fraction ϵ_e, the magnetic energy fraction ϵ_B, and the fraction of electrons accelerated in a power-law distribution by the shock ξ_N; and three observational parameters: redshift z, luminosity distance d_L, and the observer angle $\theta_{\rm obs}$ with respect to the launch direction of the fireball. Model parameters inferred from the synchrotron emission intrinsically suffer from a level of degeneracy due to the unknown ξ_N value (e.g., Eichler & Waxman 2005). We thus assume $\xi_N = 1$ as common practice in the gamma-ray burst (GRB) literature to allow a direct comparison to parameters inferred for short GRBs. We set the bounds on priors for the remaining eight parameters similar to those of Wu & MacFadyen (2018) as reported in Table 3. We perform MCMC fitting using 100 walkers and 10^4 burn-in iterations. Sampling is performed on 10^4 additional iterations. The posterior distribution of the model parameters is generated with the emcee package (Foreman-Mackey et al. 2013). The one-dimensional and two-dimensional projections of the posterior distribution that result from our fits are shown in Figure 3, and the best-fitting model is shown in Figure 1. The median values of the fitting parameters are reported in Table 3 with 1σ uncertainties computed as the 16th and 84th percentiles of the one-dimensional projection of the posterior distribution. These model parameters are consistent with those inferred by Wu & MacFadyen (2018) using data at $\delta t < 300$ days. Since the new radio and X-ray observations that we present here are consistent with the extrapolation of the model by Wu & MacFadyen (2018) at later times, this result is not surprising.

The wide distributions of E_0 and n (and ϵ_e, and ϵ_B) in Figure 3 indicates a high level of degeneracy between the model parameters. As a refinement of our modeling, we enforce the upper limit on the ambient density of GW170817 derived in Section 2.3. From the posterior distribution derived above using JetFit, we reject all the samples with $n > 9.6 \times 10^{-3}\,{\rm cm}^{-3}$, and plot the revised distribution of parameters, as shown in Figure 4, and the best-fitting model is shown in Figure 1. The median values of the revised parameter distributions are reported in Table 3. Taking the upper bound on the environment density into consideration when modeling the afterglow emission produces tighter constraints on the model parameters.

We conclude that the broadband nonthermal emission from GW170817 at ∼2 yr since merger (Figure 1) is still well described by an off-axis jetted-outflow model with angular structure. The outflow carries an explosion energy $E_0 \sim 1.5 \times 10^{49}$ erg (corresponding to an isotropic equivalent energy $E_{\rm iso} \sim 2 \times 10^{52}$ erg), with a jet opening angle $\theta_0 \sim 6°$, and characteristic Lorentz factor $\Gamma_j \sim 160$,[24] expanding in a low-density environment ($n_0 \sim 2.5 \times 10^{-3}\,{\rm cm}^{-3}$). The jet axis is located at $\theta_{\rm obs} \sim 30°$ with respect to our line of sight. Our inferences are broadly consistent with structured jet model parameters from broadband modeling attempts that included data extending to $\delta t \sim 300$ days (e.g., Lazzati et al. 2018; Mooley et al. 2018a; Ghirlanda et al. 2019; Kathirgamaraju et al. 2019b; Lamb et al. 2019; Troja et al. 2019). We find no evidence of departure from a steep post-peak lightcurve decay and we infer $F_\nu \propto t^{-1.95 \pm 0.15}$ at $\delta t > 200$ days, consistent with previous findings at earlier times (e.g., Alexander et al. 2018; Mooley et al. 2018a; Troja et al. 2019) and the expectations from emission dominated by a collimated relativistic outflow seen off-axis (Lamb et al. 2018).

The outflow will eventually enter the nonrelativistic phase at $t_{\rm NR} \propto (E_{k,{\rm iso}}/n)^{1/3}$ (e.g., Piran 2004), when the amount of swept-up material will be comparable to the kinetic energy of the outflow. The nonrelativistic transition will lead to a flattening of the lightcurve decay $F_\nu \propto t^{-\alpha}$ with $\alpha = -(15p - 21)/10 \sim 1.1$ for $\nu_m < \nu < \nu_c$ and $\alpha = -(3p - 4)/2 \sim 1.2$ above ν_c (e.g., Huang & Cheng 2003; Gao et al. 2013). For the outflow and environment density parameters listed in Table 3, the nonrelativistic transition is expected to occur at $t_{\rm NR} \sim 3600^{+2100}_{-2000}$ days ($t_{\rm NR} \sim 4700^{+1700}_{-1400}$ days for the model with the $n \leqslant 9.6 \times 10^{-3}\,{\rm cm}^{-3}$ prior). Before that happens, the KN afterglow might start dominating the observed emission (Section 5).

Table 3
JetFit Model Parameters and Inferred Quantities

Parameter	Bounds for Prior Distribution[a]	Median Value of Posterior Distribution	
		w/o Density Constraint	w/ Density Constraint
$\log_{10}E_{0,50}$ (erg)	[−6, 3]	$0.32^{+1.28}_{-1.06}$	$-0.81^{+0.53}_{-0.51}$
$\log_{10}n_0$ ($\rm cm^{-3}$)	[−6, 3]	$-1.13^{+1.27}_{-1.29}$	$-2.61^{+0.42}_{-0.63}$
$\log_{10}\epsilon_e$	[−6, 0]	$-1.64^{+1.04}_{-1.48}$	$-0.75^{+0.43}_{-0.62}$
$\log_{10}\epsilon_B$	[−6, 0]	$-4.38^{+1.59}_{-1.14}$	$-2.63^{+0.89}_{-1.23}$
η_0	[2, 10]	$8.11^{+1.27}_{-1.31}$	$8.16^{+1.18}_{-1.15}$
γ_B	[1, 12]	$8.60^{+2.10}_{-2.34}$	$9.73^{+1.38}_{-1.40}$
$\theta_{\rm obs}$ (rad)	[0, 1]	$0.58^{+0.20}_{-0.09}$	$0.53^{+0.07}_{-0.06}$
p	[2, 2.5]	$2.15^{+0.01}_{-0.02}$	$2.15^{+0.01}_{-0.02}$
Derived Quantities			
θ_0[b] (deg)		$6.66^{+2.48}_{-1.31}$	$5.89^{+0.99}_{-0.73}$
$\log_{10}E_{\rm iso,50}$[c](erg)		$3.34^{+1.33}_{-1.07}$	$2.33^{+0.60}_{-0.55}$
Γ_j[d]		139^{+39}_{-44}	163^{+23}_{-43}

Notes.
[a] The priors on the parameters are taken as uniform distribution with the given bounds.
[b] $\theta_0 \sim 1/\gamma_B$.
[c] $E_{\rm iso} \sim 2E_0/1 - \cos(\theta_0/2)$.
[d] $\Gamma_j \sim 2\eta_0\gamma_B$.

[24] The characteristic Lorentz factor of the outflow, Γ_j, mentioned here is different from Γ that we used earlier to denote the photon index of the X-ray spectra in Section 2. When mentioned in reference to the kilonova, Γ represents the Lorentz factor of the KN ejecta (as mentioned in Section 5).

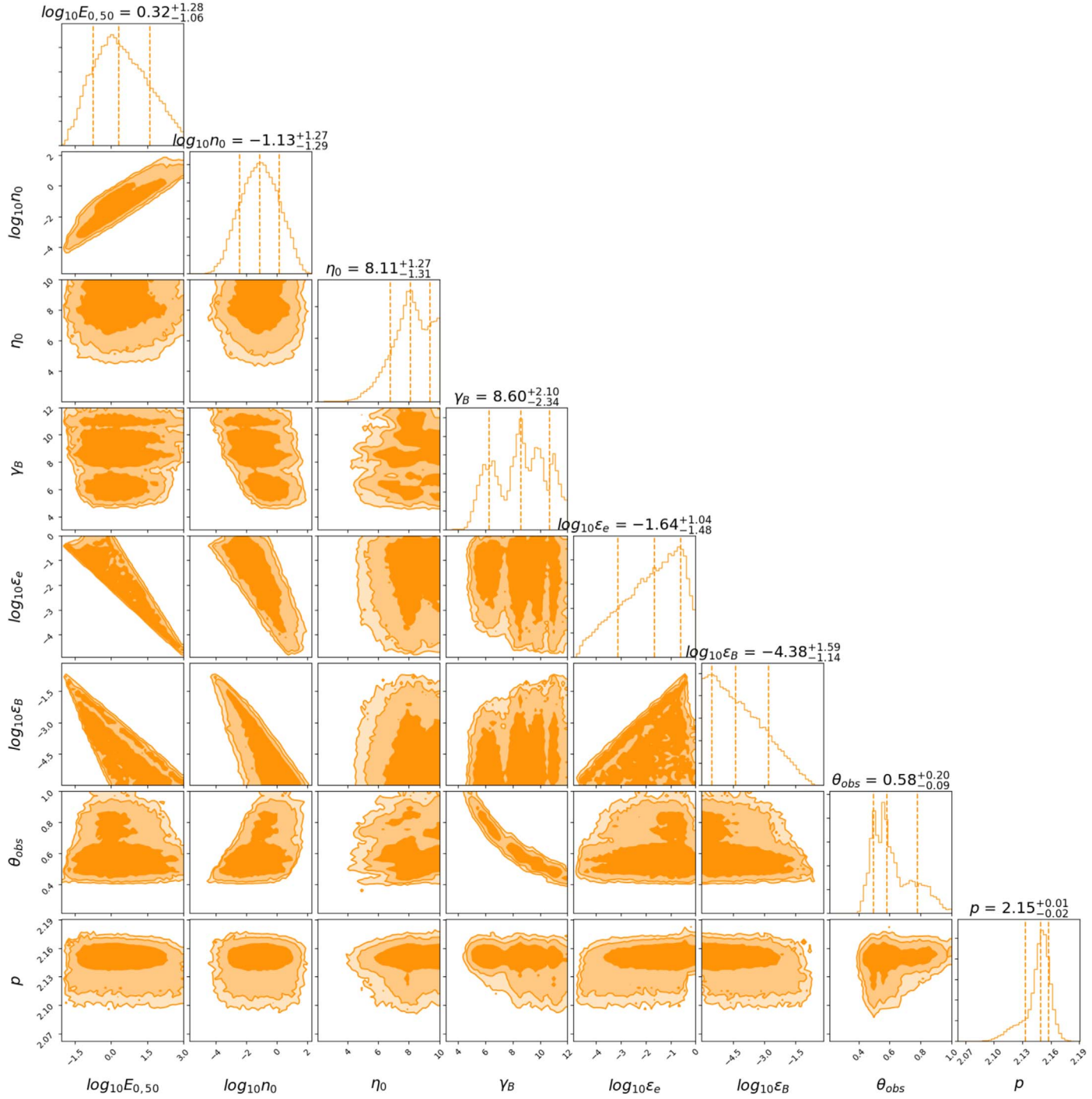

Figure 3. Corner plot showing the one- and two-dimensional projections of the posterior probability distribution of the jetted-outflow model parameters. Vertical dashed lines in the one-dimensional projections of the posterior distribution mark the 16th, 50th, and 84th percentiles of the marginalized distributions (i.e., the median value and the 1σ range). The contours are drawn at the 68%, 95%, and 99% confidence levels.

5. Constraints on the Properties of the Fastest KN Ejecta

The deceleration of the KN ejecta into the ambient medium is another source of synchrotron radiation across the electromagnetic spectrum (i.e., the KN afterglow; e.g., Nakar & Piran 2011). In close analogy to stellar explosions, the bulk of the kinetic energy in KNe is carried by "slowly" moving material that powers the detected UV–optical–NIR KN thermal emission, while the significantly lighter KN fastest ejecta rush ahead and shock the medium, accelerating electrons that cool via radiating synchrotron emission. By modeling the thermal UV–optical–NIR KN associated with GW170817, Villar et al. (2017) constrained the bulk velocities and masses of the post-merger ejecta to $v \sim 0.1$–$0.3c$ and total ejecta $M_{\rm ej} \sim 0.08\,M_{\odot}$, carrying a kinetic energy in excess of 10^{51} erg (see also Arcavi et al. 2017; Cowperthwaite et al. 2017; Drout et al. 2017; Evans et al. 2017; Kasliwal et al. 2017; Valenti et al. 2017). The KN thermal emission does not constrain the properties of the fastest KN ejecta at $\beta > 0.3\,c$ and the velocity structure $E_k^{\rm KN}(\Gamma\beta)$ of

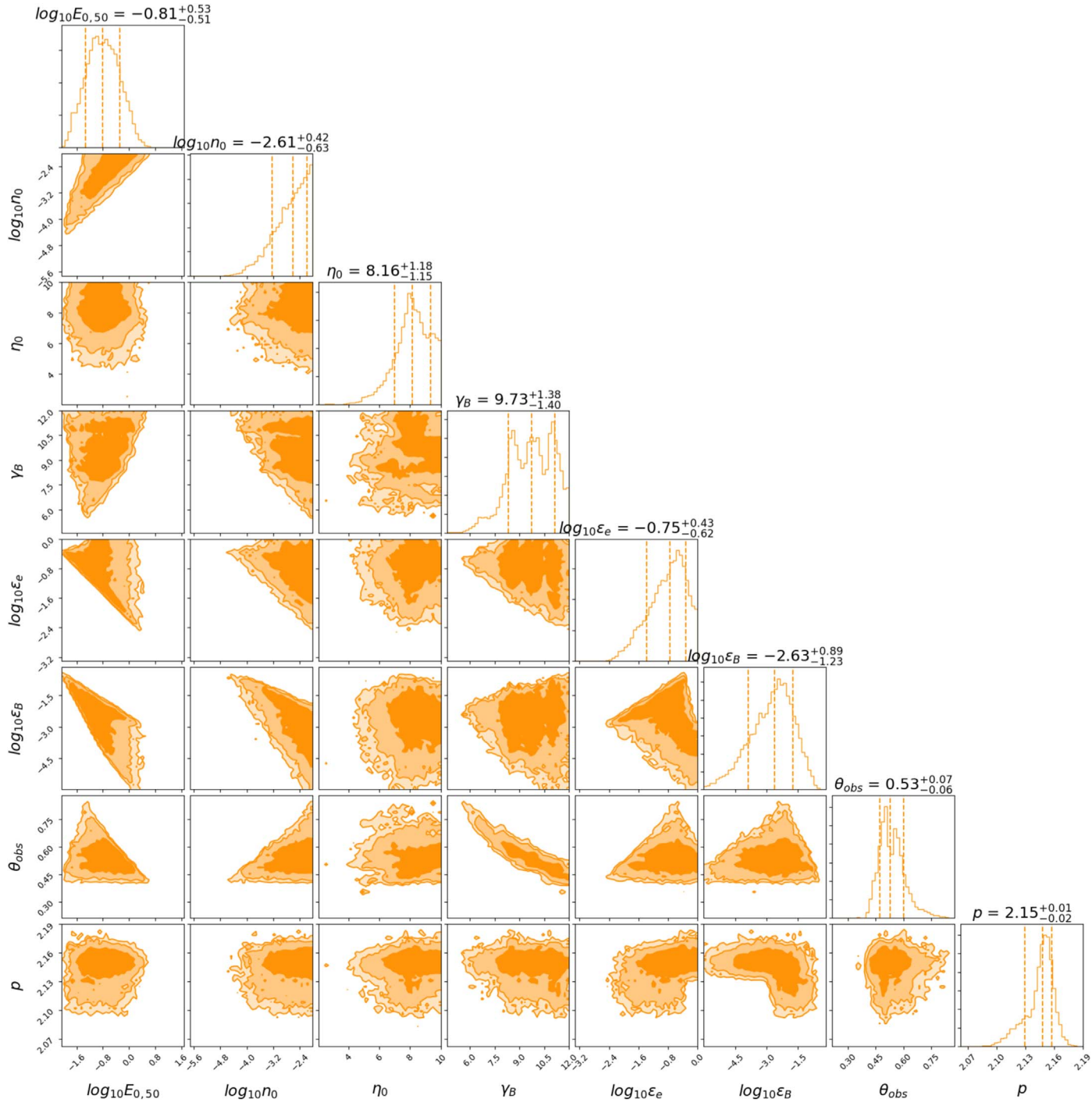

Figure 4. Same as Figure 3, but with the prior $n \leqslant 9.6 \times 10^{-3}\,\mathrm{cm}^{-3}$ as found in Section 2.3.

the KN outflow. The kinetic energy profile $E_k^{\mathrm{KN}}(\Gamma\beta)$ of the kilonova outflow carries direct information about the merger dynamics and, potentially, on the nature of the compact object remnant (e.g., Hotokezaka et al. 2018; Radice et al. 2018a, 2018b; Fernández et al. 2019).

We parameterize the kinetic energy of the fastest KN ejecta as a power law in specific momentum $\Gamma\beta$ with index α: $E_k^{\mathrm{KN}}(\Gamma\beta) \propto (\Gamma\beta)^{-\alpha}$ with a minimum outflow velocity v_0 motivated by thermal KM models. Following Kathirgamaraju et al. (2019a) we generated a set of broadband KN afterglow lightcurves with the typical parameters inferred for the afterglow of short GRBs: $v_0 = 0.3c$, total kinetic energy $\sim 10^{51}$ erg, $p = 2.2$, $\epsilon_e = 0.1$, $\epsilon_B = [10^{-4}\text{–}10^{-2}]$, $n = [10^{-4}\text{–}10^{-2}]\,\mathrm{cm}^{-3}$ (Fong et al. 2015), and with $\alpha = [3\text{–}9]$ (Radice et al. 2018a, 2018b), which are shown in Figure 1 along with the best-fitting off-axis structured jet models. We use the lack of evidence for emission from the KN afterglow to constrain the properties of the KN ejecta and its environment, as in Kathirgamaraju et al. (2019a). The results are displayed in Figure 5, which shows that current radio observations disfavor shallow stratification indices $\alpha \leqslant 6$.[25]

[25] We note that the KN afterglow and the jet afterglow do not necessarily share the same microphysical parameters ϵ_e, ϵ_B, and p as the physical properties of the shocks launched by the two outflows are different.

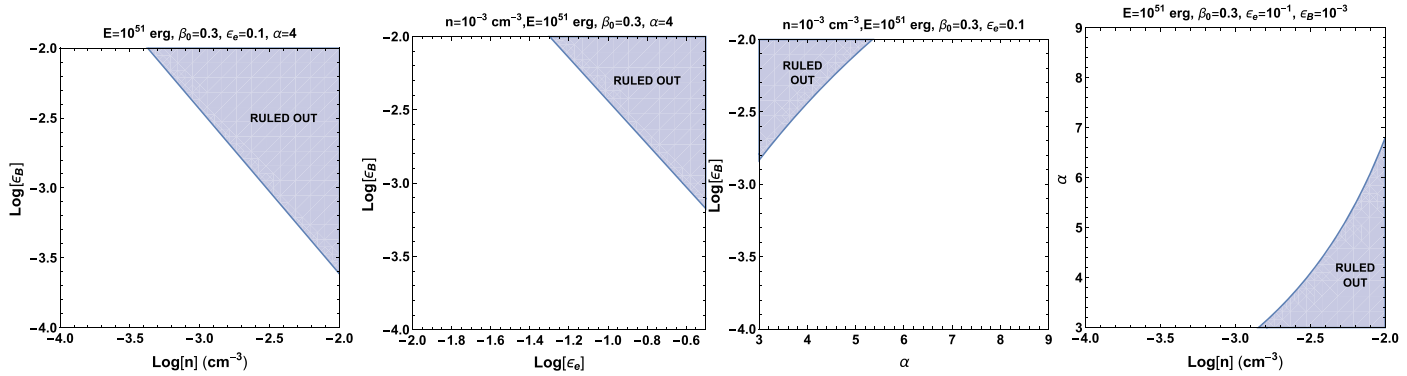

Figure 5. Allowed (white) and ruled out (shaded) parameter space of the KN afterglow of GW170817 based on the fact that no re-brightening of the X-ray or radio emission was detected at ∼2 yr after the merger (Figure 1). Two parameters are varied in each plot while the rest are kept fixed to values indicated in the plot title. The radio data set drives our conclusions and disfavors shallow stratification indexes $\alpha \leqslant 6$. Future observations will further constrain the parameter space of the KN afterglow.

Future observations at $\delta t \geqslant 1000$ days are more sensitive to the KN fastest ejecta tail and will probe a larger portion of the parameter space (Figure 1).

6. Summary and Conclusions

We present deep X-ray and radio observations of GW170817 that extend to ∼2 yr after the neutron-star merger, a homogeneous analysis of the entire X-ray data set, and a new method to independently constrain the density of the merger environment based on diffuse X-ray emission from hot plasma in the host galaxy. These observations offer a complete view of the evolution of the broadband afterglow of an off-axis structured jet launched by the neutron-star merger from its first detection at ∼10 days, peak at ∼160 days, and steep decline until the present epoch, and place the first constraints on the properties of the KN afterglow. Our main results can be summarized as follows:

1. Our analysis reveals no evidence for broadband spectral evolution or temporal variability of the X-ray emission at any time. The radio-to-X-ray data are well described by a simple power-law spectrum $F_\nu \propto \nu^{-\beta}$ with $\beta = 0.575 \pm 0.007$. The highest statistical significance of short-term temporal X-ray variability is at the level of 2.5σ.
2. From the analysis of diffuse X-ray emission from hot plasma in the host galaxy of GW170817 we infer a density limit on the NS merger environment $n \leqslant 9.6 \times 10^{-3}\,\mathrm{cm}^{-3}$. We note however that our analysis does not capture small-scale variations in density.
3. After ∼2 yr of monitoring GW170817, we conclude that the nonthermal emission from the binary neutron-star merger has been dominated at all times by a jetted outflow with angular structure viewed off-axis (Figure 1). Modeling the afterglow emission without (with) the density constraint results in $\theta_{\rm obs} = 33.2^{+11.5}_{-5.2}$ deg ($\theta_{\rm obs} = 30.4^{+4.0}_{-3.4}$ deg). The outflow carries $E = 2.1^{+38}_{-1.9} \times 10^{50}$ erg ($E = 1.5^{+3.6}_{-1.1} \times 10^{49}$ erg) of energy and contains a core of collimated ultrarelativistic material (i.e., a jet) with inferred opening angle $\theta_0 = 6.7^{+2.5}_{-1.3}$ deg ($\theta_0 = 5.9^{+1.0}_{-0.7}$ deg) and characteristic Lorentz factor $\Gamma_j = 139^{+39}_{-44}$ ($\Gamma_j = 163^{+23}_{-43}$). We infer an environment density of $n = 7.3^{+129}_{-6.9} \times 10^{-2}\,\mathrm{cm}^{-3}$ ($n = 2.5^{+4.1}_{-1.9} \times 10^{-3}\,\mathrm{cm}^{-3}$). We note that the values of opening angle, θ_0, and spectral index, p, of the electron distribution are the same in both scenarios.
4. The lack of evidence of departure from the off-axis structured jet emission allows us to constrain the properties of the yet-to-be detected KN afterglow. We find that for fiducial values of the parameters of the KN ejecta kinetic energy distribution $E_k^{\rm KN}(\Gamma\beta) \propto (\Gamma\beta)^\alpha$, current radio data disfavor shallow stratification indices $\alpha \leqslant 6$.

Future X-ray and radio observations of GW170817 have the potential to detect the very first electromagnetic signature of nonthermal emission from the deceleration of the fastest ejecta from a kilonova. Simulations show that the fastest KN ejecta is launched by a shock when the merger remnant bounces back after merger (e.g., Radice et al. 2018b). The detection of emission from a fast KN outflow would (i) confirm that a high-mass neutron star was formed that was temporarily stable to collapse, ruling out prompt black hole formation and (ii) directly provide a constraint on the neutron-star equation of state at higher densities than those probed by current LIGO/Virgo constraints on tidal deformability (as the process of "bounce" happens at higher densities and temperatures).

R.M. thanks Kenta Hotokezaka for a question at a conference that inspired the search for a new method to constrain the density in the environment of GW170817 with deep X-ray observations. The Margutti group at Northwestern acknowledges support provided by the National Aeronautics and Space Administration through grant *HST*-GO-15606.001-A, through *Chandra* Awards Number GO9-20058A, DD8-19101A and DDT-18096A issued by the *Chandra* X-ray Center, which is operated by the Smithsonian Astrophysical Observatory for and on behalf of the National Aeronautics Space Administration under contract NAS8-03060. R.M. is a CIFAR Azrieli Global Scholar in the Gravity & the Extreme Universe Program, 2019. R.M. acknowledges support by the National Science Foundation under Award No. AST-1909796. A.B. is supported by the Heising-Simons Foundation under grant #2018-0911 (PI: Margutti). A.H. is supported by a Future Investigators in NASA Earth and Space Science and Technology (FINESST) award 19-ASTRO19-0158. W.F. acknowledges support by the National Science Foundation under Award No. AST-1814782 and AST-1909358, and by the National Aeronautics and Space Administration through *Chandra* Award Number GO9-20058A issued by the *Chandra* X-ray Center, which is operated by the Smithsonian

Astrophysical Observatory for and on behalf of the National Aeronautics Space Administration under contract NAS8-03060. K.D.A. acknowledges support provided by NASA through the NASA Hubble Fellowship grant *HST*-HF2-51403.001 awarded by the Space Telescope Science Institute, which is operated by the Association of Universities for Research in Astronomy, Inc., for NASA, under contract NAS5-26555. R.C. acknowledges support from NASA *Chandra* grant GO9-20058B. This paper makes use of the following VLA data: VLA/18B-302 and VLA/SK0299. We would like to thank National Radio Astronomy Observatory for making these observations possible. The National Radio Astronomy Observatory is a facility of the National Science Foundation operated under cooperative agreement by Associated Universities, Inc.

Facilities: Chandra, VLA.

Software: HEASoft, CIAO, CASA, JetFit.

Appendix

A.1. Blind Search for Temporal Variability at $\delta t \sim 160$ *Days*

We carried out a blind search for deviations from a constant source count-rate in the time interval $\delta t = 153$–164 days for which Piro et al. (2019) report evidence for variability at the 3.3σ c.l. using two different approaches. (i) We divided the data set into two portions Δt_1 and Δt_2, where the dividing line is randomly chosen within the Δt of consideration, and we applied a Poissonian test to the number of detected photons N_1 and N_2. Our H_0 hypothesis is that N_1 and N_2 are randomly drawn from a Poisson distribution with expected rate $\lambda = 1.49 \times 10^{-3}$ c s^{-1} evaluated on the effective exposure times of the *Chandra* during Δt_1 and Δt_2 (i.e., the source count-rate is constant). We repeated the experiment 10^4 times, considering only the cases with *Chandra* exposure times during Δt_1 and Δt_2, $\Delta t_{1,\rm exp} \geqslant \Delta t_{\rm min}$, and $\Delta t_{2,\rm exp} \geqslant \Delta t_{\rm min}$, where $\Delta t_{\rm min} = 0.11$ days is such that the probability of obtaining zero photons by chance is less than $P(\geqslant 5\sigma)$ (i.e., $P(0) = e^{-\lambda \Delta t_{\rm min}} < P(\geqslant 5\sigma)$). The results from this exercise are shown in Figure 6 (red histogram). We find that a random selection of time intervals to compare typically leads to a $\sim 2\sigma$ evidence for departure from our H_0 hypothesis of a constant count-rate, consistent with our results in Section 2.1, and that only 0.3% of choices leads to a significance larger or equal to that reported by Piro et al. (2019). (ii) We further investigate the possibility of the presence of a monotonic evolution of the source count-rate, which would be best revealed by considering the initial and final portion of the data set only, as in Piro et al. (2019). We followed the same procedure as above and allowed for a random selection of the duration of the initial and final time intervals to consider within $\delta t = 153$–164 days, with the constraints $\Delta t_{1,\rm exp} \geqslant \Delta t_{\rm min}$ and $\Delta t_{2,\rm exp} \geqslant \Delta t_{\rm min}$. Figure 6 shows that only 0.4% of the 10^4 realizations that satisfy our constraints have evidence for a deviation from a constant count-rate with significance $\geqslant 3.3\sigma$, and that the typical significance is $\sim 2.2\sigma$. We conclude that the claim of a 3.3σ deviation from a constant count-rate by Piro et al. (2019) mostly stems from comparing a particular selection of time intervals, and that a blind search for temporal variability on the same data set leads to a reduced statistical significance of $\sim 2\sigma$.

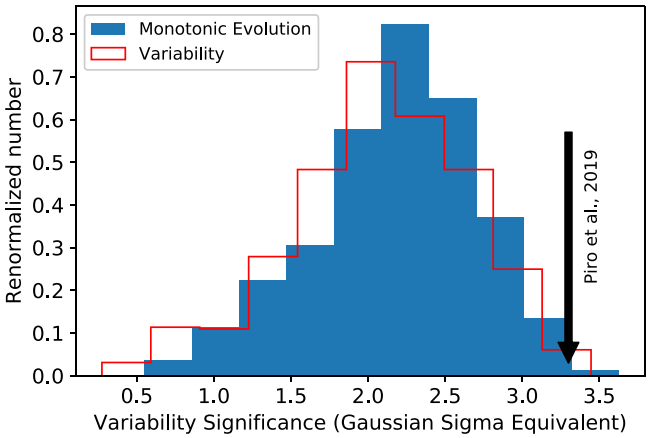

Figure 6. Distribution of statistical significance values (in units of Gaussian σ equivalent) that quantifies the evidence for deviation from the H_0 hypothesis of a source with constant count-rate between 153 and 164 days in the form of temporal variability (red), or monotonic evolution of the source count-rate (blue), for 10^4 random selections of time intervals for comparison. A limited fraction of 0.3% (red) or 0.4% (blue) of randomly selected intervals shows evidence for deviation from a constant count-rate at $\geqslant 3.3\sigma$ c.l. The typical level of significance is $\sim 2\sigma$.

ORCID iDs

R. Margutti https://orcid.org/0000-0003-4768-7586
K. D. Alexander https://orcid.org/0000-0002-8297-2473
C. Guidorzi https://orcid.org/0000-0001-6869-0835
W. Fong https://orcid.org/0000-0002-7374-935X
Y. Wu https://orcid.org/0000-0002-5347-9225
A. MacFadyen https://orcid.org/0000-0002-0106-9013
A. Paggi https://orcid.org/0000-0002-5646-2410
E. Berger https://orcid.org/0000-0002-9392-9681
P. K. Blanchard https://orcid.org/0000-0003-0526-2248
P. S. Cowperthwaite https://orcid.org/0000-0002-2478-6939
T. Eftekhari https://orcid.org/0000-0003-0307-9984
S. Gomez https://orcid.org/0000-0001-6395-6702
G. Hosseinzadeh https://orcid.org/0000-0002-0832-2974
T. Laskar https://orcid.org/0000-0003-1792-2338
B. D. Metzger https://orcid.org/0000-0002-4670-7509
M. Nicholl https://orcid.org/0000-0002-2555-3192
K. Paterson https://orcid.org/0000-0001-8340-3486
D. Radice https://orcid.org/0000-0001-6982-1008
G. Terreran https://orcid.org/0000-0003-0794-5982
V. A. Villar https://orcid.org/0000-0002-5814-4061
P. K. G. Williams https://orcid.org/0000-0003-3734-3587
X. Xie https://orcid.org/0000-0002-2798-6880
J. Zrake https://orcid.org/0000-0002-1895-6516

References

Abbott, B. P., Abbott, R., Abbott, T. D., et al. 2017a, PhRvL, 119, 161101
Abbott, B. P., Abbott, R., Abbott, T. D., et al. 2017b, ApJL, 848, L12
Alexander, K. D., Berger, E., Fong, W., et al. 2017, ApJL, 848, L21
Alexander, K. D., Margutti, R., Blanchard, P. K., et al. 2018, ApJL, 863, L18
Arcavi, I., Hosseinzadeh, G., Howell, D. A., et al. 2017, Natur, 551, 64
Asplund, M., Grevesse, N., Sauval, A. J., & Scott, P. 2009, ARA&A, 47, 481
Blanchard, P., Berger, E., Fong, W., et al. 2017, ApJL, 848, L22
Cantiello, M., Jensen, J. B., Blakeslee, J. P., et al. 2018, ApJL, 854, L31
Chornock, R., Berger, E., Kasen, D., et al. 2017, ApJL, 848, L19
Coulter, D., Foley, R., Kilpatrick, C., et al. 2017, Sci, 358, 1556
Cowperthwaite, P. S., Berger, E., Villar, V. A., et al. 2017, ApJL, 848, L17
D'Avanzo, P., Campana, S., Salafia, O. S., et al. 2018, A&A, 613, L1
Dobie, D., Kaplan, D. L., Murphy, T., et al. 2018, ApJL, 858, L15
Drout, M., Piro, A., Shappee, B., et al. 2017, Sci, 358, 1570
Duffell, P. C., & MacFadyen, A. I. 2013, ApJL, 776, L9
Eichler, D., & Waxman, E. 2005, ApJ, 627, 861
Evans, P., Cenko, S., Kennea, J., et al. 2017, Sci, 358, 1565

Fernández, R., Tchekhovskoy, A., Quataert, E., Foucart, F., & Kasen, D. 2019, MNRAS, 482, 3373
Fong, W., Berger, E., Blanchard, P. K., et al. 2017, ApJL, 848, L23
Fong, W., Berger, E., Margutti, R., & Zauderer, B. A. 2015, ApJ, 815, 102
Fong, W., Blanchard, P. K., Alexander, K. D., et al. 2019, ApJL, 883, L1
Foreman-Mackey, D., Hogg, D. W., Lang, D., & Goodman, J. 2013, PASP, 125, 306
Fruscione, A., McDowell, J. C., Allen, G. E., et al. 2006, Proc. SPIE, 6270, 62701V
Gao, H., Lei, W.-H., Zou, Y.-C., Wu, X.-F., & Zhang, B. 2013, NewAR, 57, 141
Ghirlanda, G., Salafia, O. S., Paragi, Z., et al. 2019, Sci, 363, 968
Goldstein, A., Veres, P., Burns, E., et al. 2017, ApJL, 848, L14
Granot, J., Gill, R., Guetta, D., & De Colle, F. 2018, MNRAS, 481, 1597
Haggard, D., Nynka, M., Ruan, J. J., et al. 2017, ApJL, 848, L25
Hallinan, G., Corsi, A., Mooley, K. P., et al. 2017, Sci, 358, 1579
Hotokezaka, K., Kiuchi, K., Shibata, M., Nakar, E., & Piran, T. 2018, ApJ, 867, 95
Huang, Y. F., & Cheng, K. S. 2003, MNRAS, 341, 263
Kalberla, P. M. W., Burton, W. B., Hartmann, D., et al. 2005, A&A, 440, 775
Kasliwal, M., Nakar, E., Singer, L., et al. 2017, Sci, 358, 1559
Kasliwal, M. M., Kasen, D., Lau, R. M., et al. 2019, MNRAS, in press
Kathirgamaraju, A., Giannios, D., & Beniamini, P. 2019a, MNRAS, 487, 3914
Kathirgamaraju, A., Tchekhovskoy, A., Giannios, D., & Barniol Duran, R. 2019b, MNRAS, 484, L98
Lamb, G. P., Lyman, J. D., Levan, A. J., et al. 2019, ApJL, 870, L15
Lamb, G. P., Mandel, I., & Resmi, L. 2018, MNRAS, 481, 2581
Lazzati, D., Perna, R., Morsony, B. J., et al. 2018, PhRvL, 120, 241103
Lyman, J. D., Lamb, G. P., Levan, A. J., et al. 2018, NatAs, 2, 751
Margutti, R., Alexander, K. D., Xie, X., et al. 2018, ApJL, 856, L18
Margutti, R., Berger, E., Fong, W., et al. 2017, ApJL, 848, L20
McMullin, J. P., Waters, B., Schiebel, D., Young, W., & Golap, K. 2007, in ASP Conf. Ser. 376, Astronomical Data Analysis Software and Systems XVI, ed. R. A. Shaw, F. Hill, & D. J. Bell (San Francisco, CA: ASP), 127
Mooley, K. P., Deller, A. T., Gottlieb, O., et al. 2018c, Natur, 561, 355
Mooley, K. P., Frail, D. A., Dobie, D., et al. 2018a, ApJL, 868, L11
Mooley, K. P., Nakar, E., Hotokezaka, K., et al. 2018b, Natur, 554, 207
Nakar, E., & Piran, T. 2011, Natur, 478, 82
Nicholl, M., Berger, E., Kasen, D., et al. 2017, ApJL, 848, L18
Nynka, M., Ruan, J. J., Haggard, D., & Evans, P. A. 2018, ApJL, 862, L19
Paggi, A., Fabbiano, G., Kim, D.-W., et al. 2014, ApJ, 787, 134
Piran, T. 2004, RvMP, 76, 1143
Piro, L., Troja, E., Zhang, B., et al. 2019, MNRAS, 483, 1912
Pooley, D., Kumar, P., Wheeler, J. C., & Grossan, B. 2018, ApJL, 859, L23
Radice, D., Perego, A., Hotokezaka, K., et al. 2018a, ApJL, 869, L35
Radice, D., Perego, A., Hotokezaka, K., et al. 2018b, ApJ, 869, 130
Ramirez-Ruiz, E., Andrews, J. J., & Schrøder, S. L. 2019, ApJL, 883, L6
Ruan, J. J., Nynka, M., Haggard, D., Kalogera, V., & Evans, P. 2018, ApJL, 853, L4
Savchenko, V., Ferrigno, C., Kuulkers, E., et al. 2017, ApJL, 848, L15
Troja, E., Piro, L., Ryan, G., et al. 2018, MNRAS, 478, L18
Troja, E., Piro, L., van Eerten, H., et al. 2017, Natur, 551, 71
Troja, E., van Eerten, H., Ryan, G., et al. 2019, MNRAS, 489, 1919
Valenti, S., David, J., Yang, S., et al. 2017, ApJL, 848, L24
Villar, V., Guillochon, J., Berger, E., et al. 2017, ApJL, 851, L21
Villar, V. A., Cowperthwaite, P. S., Berger, E., et al. 2018, ApJL, 862, L11
Williams, P. K. G., Clavel, M., Newton, E., & Ryzhkov, D. 2017, pwkit: Astronomical Utilities in Python, Astrophysics Source Code Library, ascl:1704.001
Wu, Y., & MacFadyen, A. 2018, ApJ, 869, 55
Wu, Y., & MacFadyen, A. 2019, ApJL, 880, L23
Xie, X., Zrake, J., & MacFadyen, A. 2018, ApJ, 863, 58